42nd AIAA Thermophysics Conference
27 - 30 June 2011, Honolulu, Hawaii

AIAA 2011-3130

Length-to-Depth Ratio Effects on Flowfield Structure of Low-Density Hypersonic Cavity Flow

Rodrigo C. Palharini* and Wilson F. N. Santos†

National Institute for Space Research, Cachoeira Paulista, SP, 12630-000, BRAZIL

A computational investigation has been carried out to examine a rarefied hypersonic flow over cavities by employing the Direct Simulation Monte Carlo (DSMC) method. The work focuses on the effects in the aerodynamic surface quantities due to variations in the cavity length-to-depth (L/H) ratio. The results presented highlight the sensitivity of the heat transfer, pressure and skin friction coefficients due to changes on the cavity L/H ratio. The L/H ratio ranged from 1 to 4, which corresponded to overall Knudsen number Kn_L in the transition flow regime. The analysis showed that the aerodynamic quantities acting on the cavity surface rely on the L/H ratio. It was found that the pressure load and the heating load to the cavity surfaces presented peak values along the frontal face, more precisely at the vicinity of the cavity shoulder. Moreover, these loads are much higher than those found in a smooth surface.

Nomenclature

a	Speed of sound, m/s
C_f	Skin friction coefficient, Eq.(5)
C_h	Heat transfer coefficient, Eq.(1)
C_p	Pressure coefficient, Eq.(3)
c	Molecular velocity, m/s
d	Molecular diameter, m
H	Cavity depth, m
Kn	Knudsen number, λ/L
L	Cavity length, m
M	Mach number, U/a
m	Molecular mass, kg
n	Number density, m^{-3}
N	Number of molecules
N_f	Dimensionless number flux, $N/n_\infty U_\infty$
p	Pressure, $\mathrm{N/m}^2$
q	Heat flux, $\mathrm{W/m}^2$
Re	Reynolds number, UL/μ
R	Reentry capsule nose radius, m
T	Temperature, K
u, v	Normal and tangential velocity components, m/s
U	Freestream velocity, m/s
x, y	Cartesian axes in physical space, m
X	Dimensionless length, x/λ_∞
Y	Dimensionless height, y/λ_∞
α	Angle of attack, degree
λ	Molecular mean free path, m
μ	Viscosity, $\mathrm{Ns/m}^2$

*Graduate Student, Combustion and Propulsion Laboratory.
†Researcher, Combustion and Propulsion Laboratory, AIAA Member.

ρ Density, kg/m^3
τ Shear stress, N/m^2
ω Viscosity index, dimensionless

Subscript
d Refers to downstream surface
u Refers to upstream surface
w Refers to wall conditions
∞ Refers to freestream conditions

I. Introduction

THERE is nowadays a rather extensive literature – mostly, but not entirely, experimental – dealing with the aerodynamic characteristics of cavities. In general, these research studies have been conducted in order to understand the physical aspects of a subsonic, supersonic or hypersonic flow past to this type of surface discontinuity.

Charwat et al.[1,2] performed a comprehensive study of a low supersonic cavity flow, $M_\infty \sim 3$. They postulated and verified the existence of an alternate emptying and filling process in the cavity. Local heat flux to the cavity floor was investigated. Their heat transfer measurements were made by a steady-state technique utilizing an estimate recovery temperature.

Nestler et al.[3] conducted an experimental investigation on cavities and steps in a hypersonic turbulent flow. For the flow conditions investigated, they found that the pressure distributions in the cavity presented a typical behavior of closed cavity flow in the sense that the flow expands into the cavity, reattaches to the floor, and separates as it approaches the downstream corner.

Unsteady hypersonic flow over cavities was investigated numerically by Morgenstern Jr. and Chokani.[4] The objective of their study was to examine the effects of Reynolds number and the cavity L/H ratio. According to the authors, relatively large heat transfer rates and static pressure variations were observed in the rear part of the cavity. In addition, flow oscillations were observed for high Reynolds number flows. Results also showed that the amplitude of these oscillations increased with the cavity L/H ratio.

The majority of the available cavity research studies in the current literature has gone into considering laminar or turbulent flow in the continuum flow regime. Nevertheless, there is little understanding of the physical aspects of hypersonic flow past to cavities related to the severe aerothermodynamic environment associated to a reentry vehicle. In this scenario, Palharini and Santos[5] have studied cavities situated in a rarefied hypersonic flow by employing the DSMC method. The work was motivated by the interest in investigating the L/H ratio effects on the flowfield structure. The primary emphasis was to examine the sensitivity of the primary properties, such as velocity, density, pressure and temperature, due to variations on the cavity L/H ratio. The analysis showed that the recirculation region inside the cavities is a function of the L/H ratio. It was found that, for $L/H < 3$, the cavity flow structure represented that one observed in a "open" cavity. Conversely, for $L/H \geq 3$, the cavity flow structure corresponded to that of a "closed" cavity. The results showed that cavity flow behavior in the transition flow regime differs from that found in the continuum flow regime, for the conditions investigated.

The present account extends further the previous analysis (Palharini and Santos[5]) by investigating the impact of the cavity L/H ratio on the aerodynamic surface quantities. In this context, the primary goal of this paper is to assess the sensitivity of the heat transfer, pressure, and skin friction coefficients for a family of cavities defined by different L/H ratio. The focus of the present study is the low-density region in the upper atmosphere. At this condition, the degree of molecular non-equilibrium is such that the Navier-Stokes equations are inappropriate. Consequently, the DSMC method will be employed to calculate the hypersonic two-dimensional flow over the cavities.

II. Geometry Definition

In the present account, the cavity length L and depth H are the same as those defined in the previous work.[5] By considering that the depth H is much smaller than the nose radius R of a reentry capsule, i.e., $H/R \ll 1$, then the hypersonic flow over the cavity may be considered as a hypersonic flow over a flat plate with a cavity. Figure 1 illustrates a schematic view of the model employed.

Referring to Fig. 1, α stands for the angle of attack, M_∞ represents the freestream Mach number, H the cavity depth, L the cavity length, L_u the length of the cavity upstream surface, and L_d the length of the cavity downstream surface. It was assumed a depth H of 0.003 m, and a length L of 0.003, 0.006, 0.009, and 0.012 m. Therefore, the cavities investigated correspond to a length-to-depth ratio, L/H, of 1, 2, 3 and 4, respectively. In addition, L_u/λ_∞ of 50 and L_d/λ_∞ of 50, where λ_∞ is the freestream molecular mean free path. It was considered that the flat plate is infinitely long but only the total length $L_u + L + L_d$ is investigated.

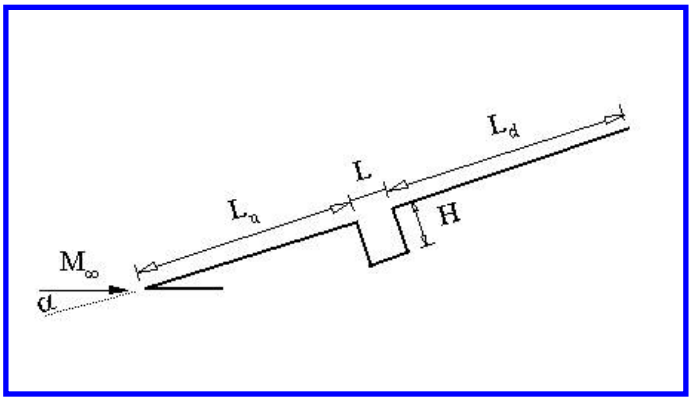

Figure 1. Drawing illustrating a schematic view of the cavity configuration.

III. Computational Method and Procedure

In order to study rarefied flow with a significant degree of non-equilibrium, the Direct Simulation Monte Carlo (DSMC) method[6] is usually employed. The DSMC method has become the most common computational technique for modeling complex transitional flows of engineering interest. The DSMC method model a gas flow by using a computer to track the trajectory of simulated particles, where each simulated particle represents a fixed number of real gas particles. The simulated particles are allowed to move, collide, and undergo boundary interactions in the simulated physical space, while the computer stores their position coordinates, velocities and other physical properties such as internal energy.

In the present account, the molecular collision kinetics are modeled by using the variable hard sphere (VHS) molecular model,[7] and the no time counter (NTC) collision sampling technique.[8] Energy exchange between kinetic and internal modes is controlled by the Borgnakke-Larsen statistical model.[9] Simulations are performed by using a non-reacting gas model, consisting of 76.3% of N_2 and 23.7% of O_2, while considering energy exchange between translational, rotational and vibrational modes. For a given collision, the probability is defined by the inverse of the number of relaxation, which corresponds to the number of collisions needed, on average, for a molecule undergoes relaxation. The probability of an inelastic collision determines the rate at which energy is transferred between the translational and internal modes after an inelastic collision. Relaxation collision numbers of 5 and 50 were used for the calculations of rotation and vibration, respectively.

IV. Computational Flow Domain and Grid

In order to facilitate the choice of molecules for collisions and for the sampling of the macroscopic flow properties, such as velocity, density, pressure, temperature, etc., the physical space around the cavity is divided into an arbitrary number of regions, which are subdivided into computational cells. The cells are further subdivided into subcells, usually two subcells/cell in each coordinate direction. In the DSMC code, the linear dimensions of the cells should be small in comparison with the scale length of the macroscopic flow gradients normal to streamwise directions, which means that the cell dimensions should be of the order of or even smaller than the local mean free path.[10,11] Furthermore, the time step should be chosen to be sufficiently small in comparison with the local mean collision time.[12,13]

The computational domain used for the calculation is made large enough so that cavity disturbances do not reach the upstream and side boundaries, where freestream conditions are specified. A schematic view of the computational domain is illustrated in Fig. 2. According to this figure, side I-A is defined by the cavity surface. Diffuse reflection with complete thermal accommodation is the condition applied to this side. Side I-B is a plane of symmetry, where all flow gradients normal to the plane are zero. At the molecular level, this plane is equivalent to a specular reflecting boundary. Sides II and III are the freestream sides through which simulated molecules can enter and exit. Side II is positioned at $5\lambda_\infty$ upstream of the flat-plate leading edge,

and side III defined at $25\lambda_\infty$ above the flat plate. Finally, the flow at the downstream outflow boundary, side IV, is predominantly supersonic and vacuum condition is specified.[6] As a result, simulated molecules can only exit at this boundary.

Numerical accuracy in DSMC method depends on the grid resolution chosen as well as on the number of particles per computational cell. Both effects were investigated to determine the number of cells and the number of particles required to achieve grid independence solutions. A grid independence study was made with three different groups of structured meshes – coarse, standard and fine – in each coordinate direction. The effect of altering the cell size in the x-direction was investigated for a coarse and fine grids with, respectively, 50% less and 100% more cells with respect to the standard grid only in the x-direction. In this fashion, a coarse, standard and fine grids corresponded to 7,500, 15,000 and 30,000 cells for the $L/H = 1$ case.

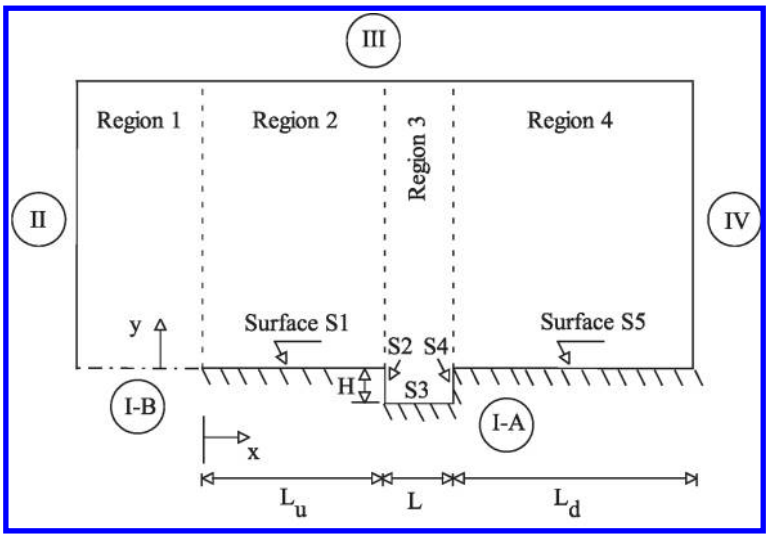

Figure 2. Drawing illustrating a schematic view of the computational domain.

In analogous fashion, an examination was made in the y-direction with coarse and fine grids with, respectively, 50% less and 100% more cells with respect to the standard grid only in the y-direction. In addition, each grid was made up of non-uniform cell spacing in both directions. Moreover, point clustering is used close to solid walls and to the horizontal plane connecting the two corners. The effect (not shown) of changing the cell size in both directions on the heat transfer, pressure and skin friction coefficients was rather insensitive to the range of cell spacing considered, indicating that the standard grid, with a total of 15,000 cells, for the $L/H = 1$ case, is essentially grid independent.

A similar examination was made for the number of molecules. The standard grid for the $L/H = 1$ case corresponds to, on average, a total of 314,700 molecules. Two new cases using the same grid were investigated. These two new cases correspond to 157,500 and 630,600 molecules in the entire computational domain. As the three cases presented the same results (not shown) for the heat transfer, pressure and skin friction coefficients, hence the standard grid with a total of 314,700 molecules was considered enough for the computation of the flowfield properties. A discussion of the effects of the cell size, time step, and number of molecules variations on the aerodynamic surface quantities for the cavities presented herein is described in detail by Palharini.[14]

V. Freestream and Flow Conditions

Freestream flow conditions used for the numerical simulations are those given by Palharini and Santos[5] and summarized in Tab. 1. Gas properties, such as mass fraction, molecular mass, molecular diameter and viscosity index, associated with the working fluid, N_2 and O_2, are given by Bird.[6] Freestream conditions represent those experienced by a capsule at an altitude of 70 km. This altitude is associated with the transition flow regime, which is characterized by the overall Knudsen number the order of or larger than 10^{-2}. Referring to Tab. 1, T_∞, p_∞, ρ_∞, μ_∞, n_∞, λ_∞, and U_∞ stand, respectively, for temperature, pressure, density, viscosity, number density, molecular mean free path, and velocity.

Table 1. Freestream flow conditions

Altitude (km)	T_∞(K)	p_∞(N/m^2)	ρ_∞(kg/m^3)	μ_∞(Ns/m^2)	n_∞(m^{-3})	λ_∞(m)
70	220.0	5.582	8.753×10^{-5}	1.455×10^{-5}	1.8209×10^{21}	9.03×10^{-4}

The freestream velocity U_∞, assumed to be constant at 7456 m/s, corresponds to a freestream Mach number M_∞ of 25. The wall temperature T_w is assumed constant at 880 K. This temperature is chosen to be representative of the surface temperature near the stagnation point of a reentry capsule and is assumed to be uniform over the cavity surface. It is important to mention that the surface temperature is low compared to the stagnation temperature of the air. For the present account, the ratio of surface temperature to the stagnation temperature is around 0.032.

Table 2. Gas properties

	X	m (kg)	d (m)	ω
O_2	0.237	5.312×10^{-26}	4.01×10^{-10}	0.77
N_2	0.763	4.650×10^{-26}	4.11×10^{-10}	0.74

The degree of rarefaction of a flow is usually expressed through the overall Knudsen number, $Kn = \lambda/l$, where λ is the mean free path in the freestream gas and l is a characteristic length of the flowfield. By assuming the cavity length L as the characteristic length, the overall Knudsen number Kn_L corresponds to 0.3095, 0.1548, 0.1032, and 0.0774 for length L of 0.003, 0.006, 0.009, and 0.012 m, respectively. In addition, the Reynolds number Re_L is around 121.7, 243.4, 365.1, and 486.8 for length L of 0.003, 0.006, 0.009, and 0.012 m, respectively, also based on conditions in the undisturbed stream. Finally, it was assumed a zero-degree angle of attack.

VI. Computational Results and Discussion

It is the purpose of this section to discuss and to compare some differences in the aerodynamic surface quantities due to changes on the cavity L/H ratio. Surface quantities of particular interest in the present account are number flux, heat flux, wall pressure and shear stress.

Before proceeding with the analysis of the aerodynamic surface quantities, it proves instructive to present first the flow topology inside the cavities. In doing so, density ratio, ρ/ρ_∞, contours with streamline traces inside the cavities are demonstrated in Fig. 3 for L/H ratio of 1, 2, 3 and 4. In this group of diagrams, Y_H stands for the vertical distance y normalized by the cavity depth H, and X'_H is the length $(x - L_u)$ also normalized by the cavity depth H.

According to Fig. 3, it is clearly noticed that the flow inside cavities is characterized by the appearance of recirculation regions. The streamline pattern for the L/H ratio of 1 and 2 shows that the flow is characterized by a primary vortex system, and the recirculating structure fills the entire cavity. In the following, for the $L/H = 3$ case, a different flow structure is observed; two vortices are formed, one of them closed to the back face (upstream face) and the other one at the vicinity of the frontal face (downstream face) of the cavity. The external stream does not reattach and the flow is reversed along all the floor of the cavity. Finally, for the $L/H = 4$ case, the recirculation regions are well defined when compared to the previous case. In addition, for this particular case, the external stream reattaches the cavity floor.

A. Number Flux

The number flux, N, is calculated by sampling the molecules impinging on the surface by unit time and unit area. The distribution of the number flux along the surfaces S1, S2, S3, S4 and S5 (as defined in Fig. 2) is illustrated in Figs. 4 and 5 as a function of the L/H ratio. In this group of plots, N_f represents the number flux N normalized by $n_\infty U_\infty$, where n_∞ and U_∞ correspond, respectively, to the freestream number density and freestream velocity. Also, X stands for the length x normalized by the freestream mean free path λ_∞, X' refers to the length $(x - L_u)$ normalized by the cavity length L, and Y_H refers to the height y normalized by the cavity depth H. As a basis of comparison, the dimensionless number flux N_f for the flat-plate case, i.e., a flat plate without a cavity, is also illustrated in Figs. 4 and 5.

Looking first at Fig. 4, it is seen that the dimensionless number flux N_f to the surfaces basically does not depend on the L/H ratio, for the conditions investigated. From the leading edge up to a station close to the cavity location ($X = 50$), the number flux behavior for the cavities is similar to that for the flat-plate case, i.e., a plate without a cavity. This is an expected behavior in the sense that this region is not affected by the presence of the cavities. However, close to the upstream cavity shoulder, i.e., the surface-S1/surface-S2 junction, there is a decrease in the number flux due to the flow expansion around the upstream shoulder. A magnified view of this behavior is shown in detail in the middle plot. Along the surface S5, right plot,

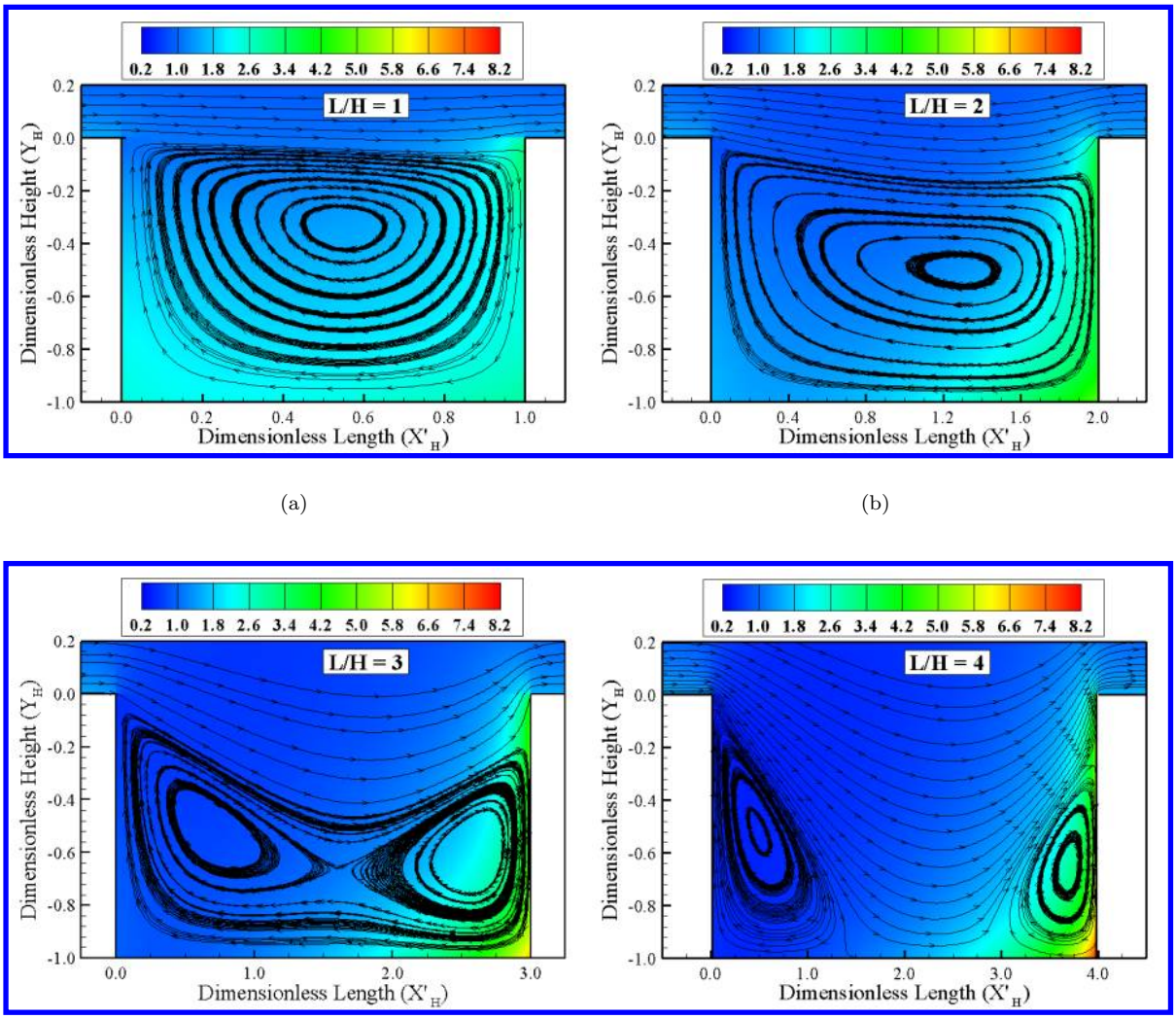

Figure 3. Density ratio ρ/ρ_∞ contours with streamline traces inside the cavities for L/H ratio of (a) 1, (b) 2, (c) 3, and (d) 4.

it is seen that the dimensionless number flux N_f behavior is similar to that for the flat-plate case, except at the vicinity of the downstream shoulder, i.e., the surface-S4/surface-S5 junction. It should be remarked that the total length of the flat plate is equal to the largest cavity, i.e., the $L/H = 4$ case. It should be also mentioned that the significant number-flux drop at the end of the curves is due to the vacuum condition assumed to the downstream outflow boundary, side IV in the computational domain.

Turning next to Fig. 5, it is clearly noticed that the number flux N_f to the surfaces S2, S3 and S4 relies on the cavity L/H ratio. Along the backward face, surface S2, the dimensionless number flux is low at the top of the cavity, and increases monotonically along the surface up to the corner at the bottom surface. Conversely, for the forward face, surface S4, the dimensionless number flux depends on the L/H ratio. For the $L/H = 1$ case, the number flux is high at the shoulder of the cavity, $Y_H = 0$, and decreases to a minimum value at the bottom surface. For the $L/H > 1$ cases, the number flux N_f basically starts increasing at the shoulder, $Y_H = 0$, slightly decreases up to the station $Y_H \approx$ -0.7, and increases again along the surface up to the corner at the bottom surface. Along the bottom surface, surface S3, the dimensionless number flux behavior also depends on the L/H ratio. It basically increases from one corner to another one with

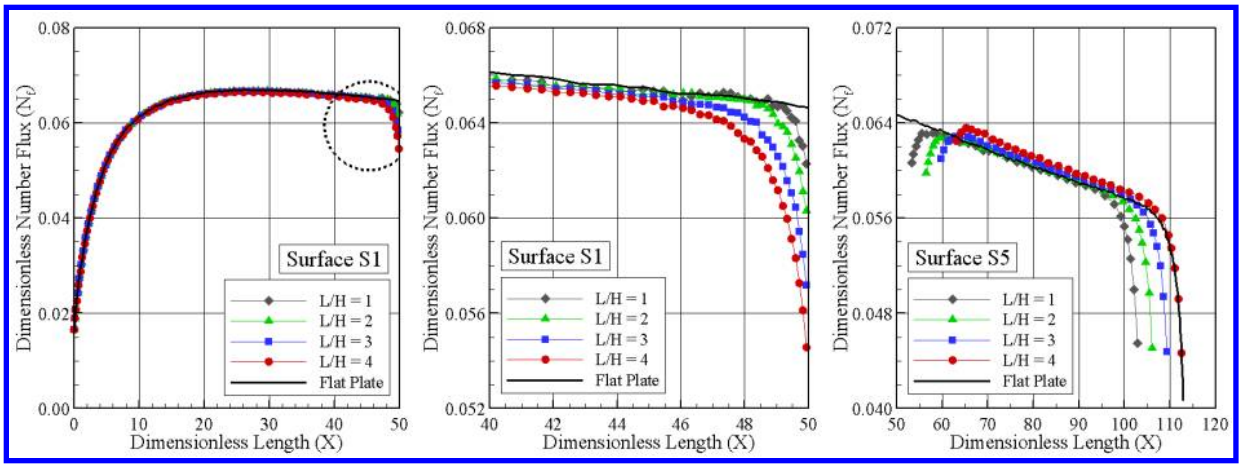

Figure 4. Distribution of dimensionless number flux N_f along the cavity surfaces S1 (left) and S5 (right), along with a magnified view of the curves at the vicinity of the cavity shoulder (middle).

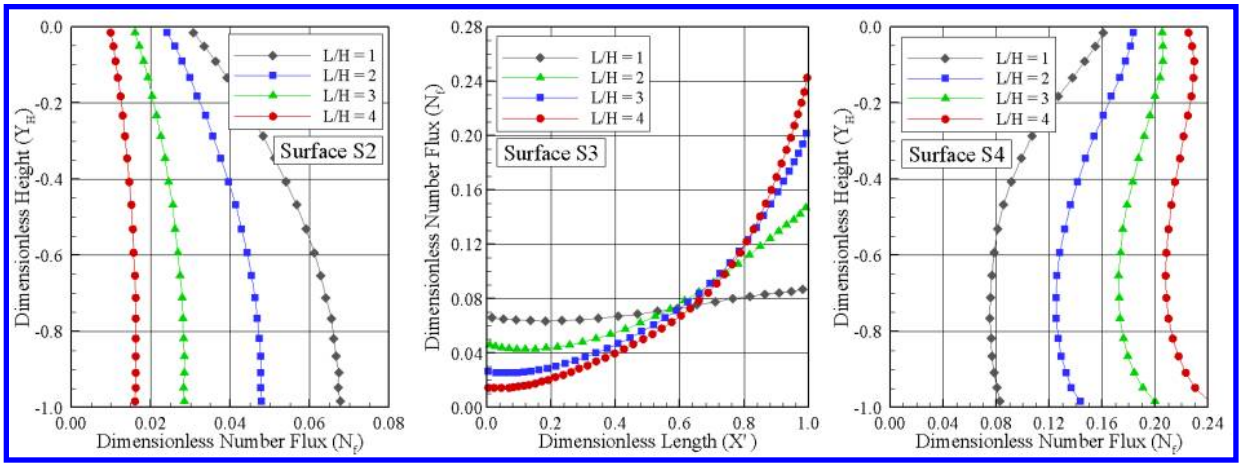

Figure 5. Distribution of dimensionless number flux N_f along the cavity surfaces S2 (left), S3 (middle), and S4 (right).

increasing the L/H ratio.

It may be recognized from Fig. 5 that, in general, the dimensionless number flux N_f along the forward face, surface S4, is one order of magnitude larger than that along the backward face, surface S2. An understanding of this behavior can be gained by considering the flow structure inside the cavities, as shown in Fig. 3. Due to the clockwise recirculation region inside the cavities, density is low at the vicinity of the backward face. In contrast, density is high at the vicinity of the forward face, since the flow experiences a compression.[5] Consequently, the number flux behavior is different along the two surfaces.

B. Heat Transfer Coefficient

The heat transfer coefficient C_h is defined as follows,

$$C_h = \frac{q_w}{\frac{1}{2}\rho_\infty U_\infty^3} \tag{1}$$

where the heat flux q_w to the body surface is calculated by the net energy flux of the molecules impinging on the surface. A flux is regarded as positive if it is directed toward the body surface. The net heat flux q_w is related to the sum of the translational, rotational and vibrational energies of both incident and reflected molecules as defined by,

$$q_w = q_i - q_r = \frac{F_N}{A\Delta t}\{\sum_{j=1}^{N}[\frac{1}{2}m_j c_j^2 + e_{Rj} + e_{Vj}]_i - \sum_{j=1}^{N}[\frac{1}{2}m_j c_j^2 + e_{Rj} + e_{Vj}]_r\} \quad (2)$$

where F_N is the number of real molecules represented by a single simulated molecule, Δt is the time step, A the area, N is the number of molecules colliding with the surface by unit time and unit area, m is the mass of the molecules, c is the velocity of the molecules, e_R and e_V stand for rotational and vibrational energies, respectively. Subscripts i and r refer to incident and reflect molecules.

The sensitivity of the heat transfer coefficient C_h along the cavity surfaces, S1, S2, S3, S4 and S5, is demonstrated in Figs. 6 and 7 as a function of the L/H ratio. According to Fig. 6, no appreciable changes are observed in the heat transfer coefficient C_h along the surface S1 due to the L/H ratio rise. Similar to the dimensionless number flux, it is seen that the heat transfer coefficient along the surface S1 exhibits the same behavior for the flat-plate case from the leading edge up to near the upstream corner of the cavities. For the range of L/H investigated, C_h is low at the leading edge, increases to a peak value, $C_h = 0.0285$ at section $X = 8.82$, and then decreases downstream up to the cavity upstream shoulder, i.e., surface-S1/surface-S2 junction. Particular attention is paid to the upstream disturbance due to the presence of the cavities. It is observed that the extension of the upstream disturbance in the heat transfer coefficient is much less than that observed for the number flux. This behavior is elucidated in the magnified view presented in the middle plot in Fig. 6.

Still referring to Fig. 6, along the surface S5, it is observed that the heat transfer coefficient C_h is larger than that for the flat-plate case, especially in the vicinity of the downstream corner of the cavity, defined by the surface-S4/surface-S5 junction. Nevertheless, as the flow moves downstream along the surface, the heat transfer coefficient C_h basically recovers the value obtained for the flat-plate case.

According to Fig. 7, for the backward face, surface S2, the heat transfer coefficient C_h is low at the cavity shoulder, $Y_H = 0$, and increases to a maximum value close to the station $Y_H \approx$ -0.4. Afterwards, it decreases along the surface up to the corner at the bottom surface. Along the cavity floor, surface S3, the heat transfer coefficient depends on the L/H ratio. C_h roughly increases from zero, at station $X' = 0$, and reaches a maximum value around station $X' = 0.85$. In addition, the larger the L/H ratio is the larger the maximum value attained by the heat transfer coefficient C_h. After that, C_h drops off up to the surface-S3/surface-S4 junction. For the forward face, surface S4, the heat transfer coefficient C_h is high at the top of the cavity,

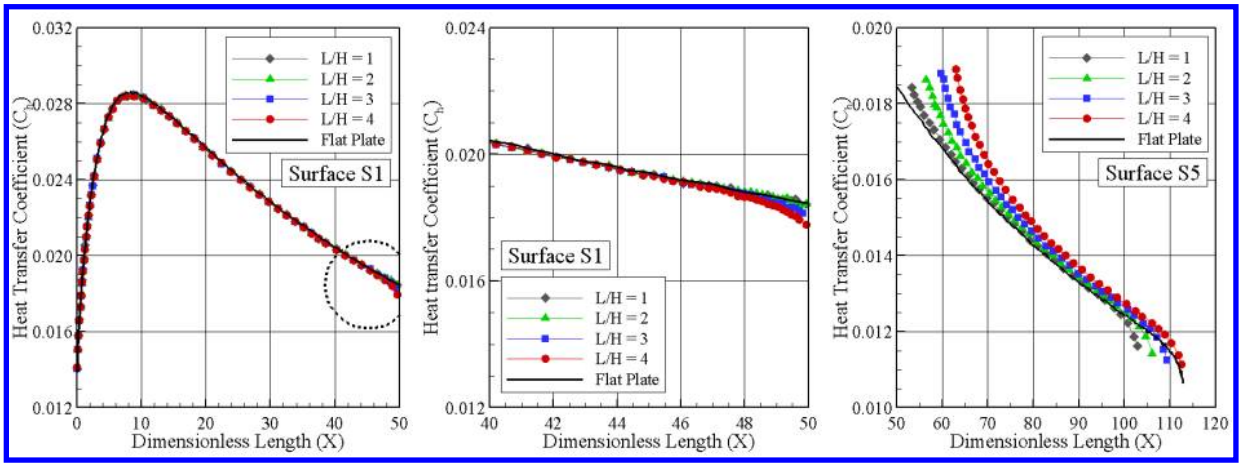

Figure 6. Distribution of heat transfer coefficient C_h along the cavity surfaces S1 (left) and S5 (right), along with a magnified view of the curves at the vicinity of the cavity shoulder (middle).

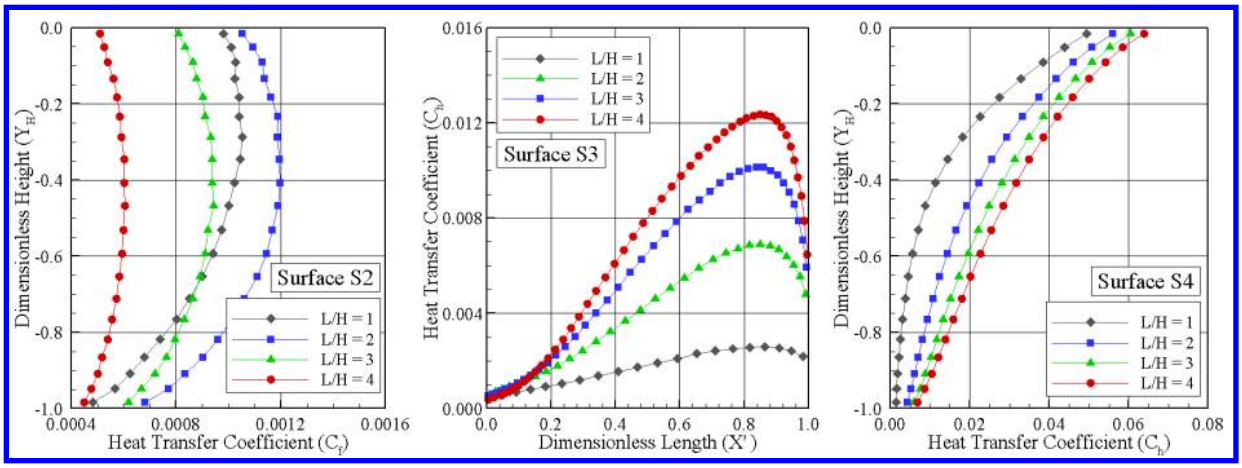

Figure 7. Distribution of heat transfer coefficient C_h along the cavity surfaces S2 (left), S3 (middle), and S4 (right).

and monotonically decreases along the surface, reaching very lower values at the corner. It is also very encouraging to observe that the peak values for the heat transfer coefficient C_h to the forward face is one order of magnitude larger than that for the upstream face. One possible reason for that is because at the vicinity of the backward face the flow experiences a expansion. In contrast, at the vicinity of the forward face, it experiences a compression due to the recirculation structure inside the cavity (Fig. 3).

At this point it is worth taking a closer look at these results. In order to do that, the peak values for the heat transfer coefficient C_h, approximately 0.049, 0.056, 0.060, and 0.064 for the L/H ratio of 1, 2, 3, and 4, respectively, at the cavity shoulder, are compared to that predicted for a smooth surface, i.e., a flat plate without a cavity. Based on Fig. 7, the maximum value for C_h is around to 0.0284 at a station $9.11\lambda_\infty$ from the leading edge. Therefore, the C_h peak value for the cavities is more than twice of that for a smooth surface.

C. Pressure Coefficient

The pressure coefficient C_p is defined as follows,

$$C_p = \frac{p_w - p_\infty}{\frac{1}{2}\rho_\infty U_\infty^2} \tag{3}$$

where the pressure p_w on the body surface is calculated by the sum of the normal momentum fluxes of both incident and reflected molecules at each time step as follows,

$$p_w = p_i - p_r = \frac{F_N}{A\Delta t}\sum_{j=1}^{N}\{[(mv)_j]_i - [(mv)_j]_r\} \tag{4}$$

where v is the velocity component of the molecule j in the surface normal direction.

The effect on the pressure coefficient C_p due to variation in the L/H ratio is depicted in Fig. 8 for surfaces S1 and S5, and in Fig. 9 for surfaces S2, S3 and S4. Referring to Fig. 8, it is observed that the pressure coefficient follows the same trend as that presented for the dimensionless number flux in the sense that, along the surface $S1$, the pressure coefficient displays the same behavior as that for the flat-plate case. From the leading edge up to a station close to the cavity location ($X = 50$), the pressure coefficient behavior for the cavities is similar to that for the flat-plate case. Again, close to the upstream cavity shoulder, i.e., the surface-S1/surface-S2 junction, a significant reduction in the pressure coefficient is observed when compared to the pressure coefficient of the flat-plate case. As mentioned earlier, the reason for that is due

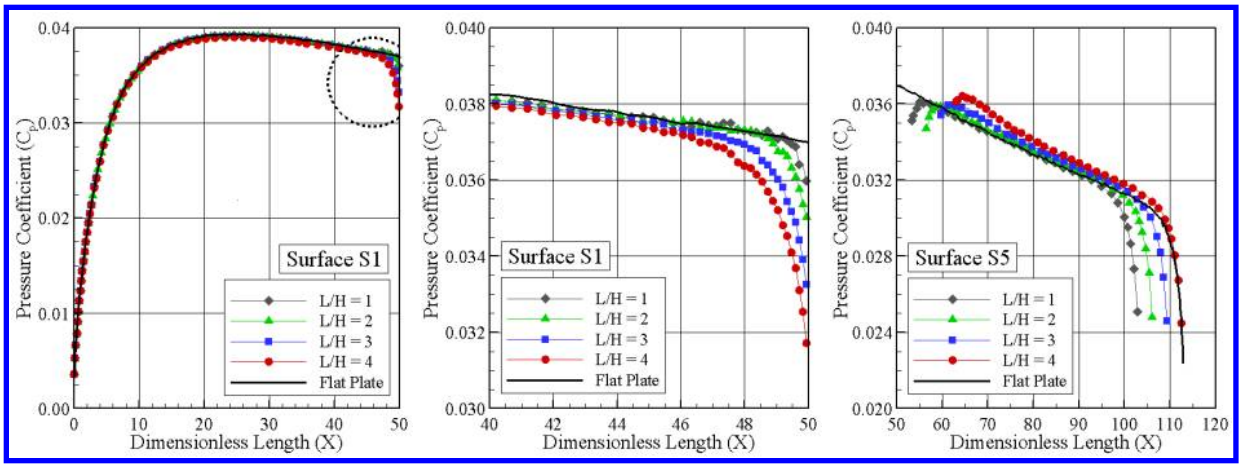

Figure 8. Distribution of pressure coefficient C_p along the cavity surfaces S1 (left) and S5 (right), along with a magnified view of the curves at the vicinity of the cavity shoulder (middle).

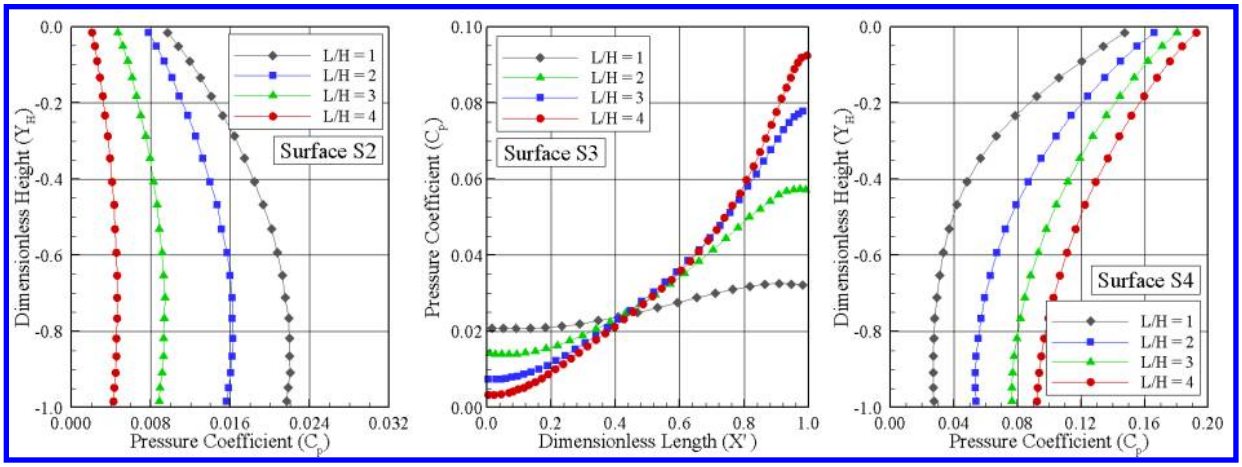

Figure 9. Distribution of pressure coefficient C_p along the cavity surfaces S2 (left), S3 (middle), and S4 (right).

to the flow expansion around the upstream shoulder. This behavior is shown in detail in a magnified view, the middle plot in Fig. 8. Along the surface S5, right plot, it is observed that the pressure coefficient C_p behavior is similar to that for the flat-plate case, except at the vicinity of the downstream shoulder, i.e., the surface-S4/surface-S5 junction.

According to the Fig. 9, it is seen that the pressure coefficient C_p roughly follows a similar behavior as that presented by the number flux in the sense that, for the backward face, surface S2, it is low at the shoulder, $Y' = 0$, and increases downward along the surface, reaching the maximum value at the bottom, station Y_H = -1.0. In the following, for the cavity floor, surface S3, the pressure coefficient C_p increases along the entire surface, and reaches the maximum value at the vicinity of the surface-S3/surface-S4 junction. Finally, along the forward face, surface S4, the pressure coefficient behavior is in contrast to that observed along the surface S2 in the sense that C_p presents the lower value at the station $Y_H = -1.0$, and increases monotonically upward along the surface, reaching the peak value at the shoulder, $Y_H = 0$. It may be inferred in passing that this is an expected behavior since the flow within the cavity is characterized by the appearance of a recirculation region. According to Palharini and Santos,[5] the streamline pattern shows that the flow is characterized by a primary vortex system for $L/H = 1$ and 2 cases, where a clockwise recirculation structure fills the entire

cavities. Conversely, for the $L/H = 3$ and 4 cases, the flow is characterized by two vortex systems at the vicinity of the backward and forward surfaces, with the freestream flow reaching the cavity floor, surface S3.

In the following, it proves helpful to compare the maximum values for the pressure coefficient observed in the cavities with that of a smooth surface, i.e., a flat plate without a cavity. As a basis of comparison, for the $L/H = 4$ case, the pick values for C_p is around 0.092 and 0.193 observed at the cavity floor, surface S3, and at the cavity shoulder, surface S4, respectively. Based on Fig. 8, for the flat-plate case, the maximum value for C_p is around to 0.0393 at a station $25.9\lambda_\infty$ from the leading edge. Therefore, the C_p peak value for the largest cavity is around 2.3 and 4.9 times larger than the peak value for a smooth surface.

D. Skin Friction Coefficient

The skin friction coefficient C_f is defined as follows,

$$C_f = \frac{\tau_w}{\frac{1}{2}\rho_\infty U_\infty^2} \tag{5}$$

where the shear stress τ_w on the body surface is calculated by the sum of the tangential momentum fluxes of both incident and reflected molecules impinging on the surface at each time step by the following expression,

$$\tau_w = \tau_i - \tau_r = \frac{F_N}{A\Delta t}\sum_{j=1}^{N}\{[(mu)_j]_i - [(mu)_j]_r\} \tag{6}$$

where u is the velocity component of the molecule j in the surface tangential direction.

It is worthwhile to note that for the special case of diffuse reflection, the gas-surface interaction model adopted in present work, the reflected molecules have a tangential moment equal to zero, since the molecules essentially lose, on average, their tangential velocity components. In this fashion, the contribution of τ_r in Eq. 6 is equal to zero.

The impact on the skin friction coefficient C_f due to changes on the cavity L/H ratio is demonstrated in Fig. 10, for surfaces S1 and S5, and in Fig. 11, for surfaces S2, S3, and S4. According to Fig. 10, it is firmly established that the skin friction coefficient C_f follows a similar behavior of that presented by the heat transfer coefficient C_h. Along the surface S1, it is observed that C_f reproduces the skin friction distribution for the flat-plate case. In addition, broadly speaking, no upstream disturbance due to the presence of the cavities is observed, as is apparent from the magnified view in the middle plot. Along the surface S5, similar to the heat transfer coefficient, it is noticed that the skin friction coefficient C_f is larger than that for the flat-plate case, especially in the vicinity of the downstream corner of the cavity, defined by the surface-S4/surface-S5 junction. However, as the flow moves downstream along the surface, the skin friction coefficient C_f basically recovers the value observed for the flat-plate case. Finally, it may be observed that the peak values for the skin friction coefficient along surfaces S1 and S5 are larger than those observed for the pressure coefficient. As a result, tangential forces, associated to the shear stress, are larger than normal forces, related to the wall pressure.

Turning next to Fig. 11, for the backward face, surface S2, it is observed that the skin friction coefficient presents the peak value at the shoulder, $Y_H = 0$, then it decreases downward along the surface up to station $Y_H \approx$ -0.75, and becomes negative along the remaining part of the surface. In what follows, for the cavity floor, surface S3, the skin friction coefficient behavior relies on the L/H ratio. It is negative near to the vicinity of the surface-S2/surface-S3 junction, then it becomes positive and reaches a maximum value as a function of the L/H ratio. Along the forward face, surface S4, the skin friction coefficient increases negatively upward along the entire surface.

Usually, as C_f changes from positive to negative value, the condition $C_f = 0$ may indicate the presence of a backflow, an attachment or a reattachment point in a 2-D flow. In the present account, these changes are directly related to the clockwise recirculation structure, defined by a primary vortex system observed for the $L/H = 1$ and 2 cases, and two recirculating structures observed for the $L/H = 3$ and 4 cases, where the flow is characterized by two vortex system at the vicinity of the backward and forward faces. As a result, the skin friction coefficient distribution along the bottom surface, S3, is similar for the $L/H = 1$ and 2 cases. In addition, the distribution for the $L/H = 3$ case presents a similar behavior as that for the $L/H = 4$ case.

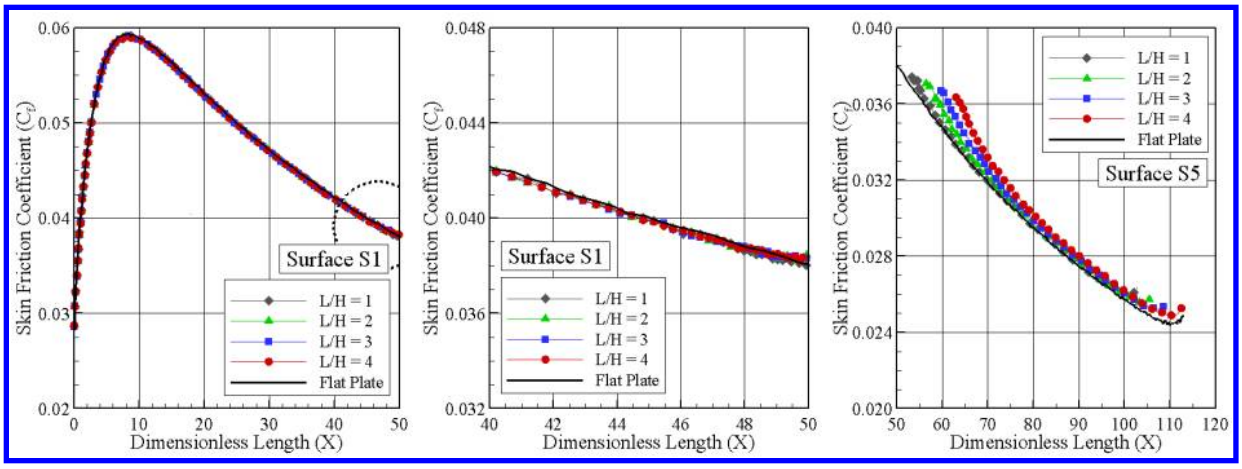

Figure 10. Distribution of skin friction coefficient C_f along the cavity surfaces S1 (left) and S5 (right), along with a magnified view of the curves at the vicinity of the cavity shoulder (middle).

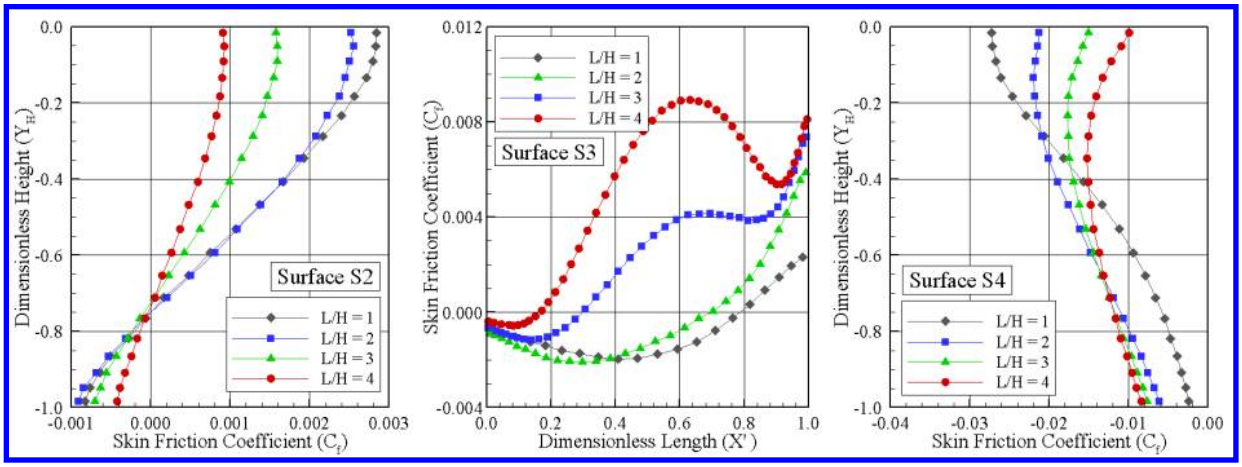

Figure 11. Distribution of skin friction coefficient C_p along the cavity surfaces S2 (left), S3 (middle), and S4 (right).

VII. Concluding Remarks

A detailed numerical study has been carried out to investigate a rarefied hypersonic flow over cavities using the Direct Simulation Monte Carlo (DSMC) method. The simulations provided information about the aerodynamic properties on the cavities surfaces. Effects of the length-to-depth ratio on the number flux, heat transfer, pressure, and skin friction coefficients were investigated.

The analysis showed that the aerodynamic quantities acting on the cavity surface depend on the L/H ratio. It was found that the pressure load and the heat flux to the cavity surface exhibited maximum values along the forward face, more precisely at the vicinity of the cavity shoulder. In addition, these loads are much higher than the maximum values found for a smooth surface, i.e., a flat plate without cavities. Consequently, in a hypersonic vehicle design, pressure and thermal loads become important if discontinuities, such as cavities, are present in the vehicle surface.

VIII. Acknowledgments

The authors would like to thank the financial support provided by FAPESP (Fundação de Amparo a Pesquisa do Estado de São Paulo) under Grant No. 2007/57673-6.

References

[1]Charwat, A. F., Dewey, C. F., Roos, and J. N, Hitz, J. A., "An Investigation of Separated Flows – Part I: The Pressure Field", *Journal of Aerospace Sciences*, Vol. 28, No. 6, 1961, pp. 457–470.

[2]Charwat, A. F., Dewey, C. F., Roos, and J. N, Hitz, J. A., "An Investigation of Separated Flows – Part II: Flow in the Cavity and Heat Transfer", *Journal of Aerospace Sciences*, Vol. 28, No. 7, 1961, pp. 513–527.

[3]Nestler, D. E., Saydah, A. R., and Auxer, W. L., "Heat Transfer to Steps and Cavities in Hypersonic Turbulent Flow", *AIAA Journal*, Vol. 7, 1969, pp. 1368–1370.

[4]Morgenstern Jr., A., and N. Chokani, N., "Hypersonic Flow Past Open Cavities", *AIAA Journal*, Vol. 32, 1994, pp. 2387–2393.

[5]Palharini, R. C.,and Santos, W. F. N., "Computational Analysis of Hypersonic Flow over Cavities", *3rd Southern Conference on Computational Modeling*, nov 23–25, 2010, Rio Grande-RS, Brazil.

[6]Bird, G. A.,*Molecular Gas Dynamics and the Direct Simulation of Gas Flows*, Oxford University Press, Oxford, England, UK, 1994.

[7]Bird, G. A., "Monte Carlo Simulation in an Engineering Context," in *Progress in Astronautics and Aeronautics: Rarefied gas Dynamics*, edited by Sam S. Fisher, Vol. 74, part I, AIAA New York, 1981, pp. 239–255.

[8]Bird, G. A., "Perception of Numerical Method in Rarefied Gasdynamics," in *Rarefied gas Dynamics: Theoretical and Computational Techniques*, edited by E. P. Muntz, and D. P. Weaver and D. H. Capbell, Vol. 118, Progress in Astronautics and Aeronautics, AIAA, New York, 1989, pp. 374–395.

[9]Borgnakke, C. and Larsen, P. S., "Statistical Collision Model for Monte Carlo Simulation of Polyatomic Gas Mixture," *Journal of computational Physics*, Vol. 18, No. 4, 1975, pp. 405–420.

[10]Alexander, F. J., Garcia, A. L., and, Alder, B. J., "Cell Size Dependence of Transport Coefficient in Stochastic Particle Algorithms," *Physics of Fluids*, Vol. 10, No. 6, 1998, pp. 1540–1542.

[11]Alexander, F. J., Garcia, A. L., and, Alder, B. J., "Erratum: Cell Size Dependence of Transport Coefficient is Stochastic Particle Algorithms," *Physics of Fluids*, Vol. 12, No. 3, 2000, pp. 731–731.

[12]Garcia, A. L., and, Wagner, W., "Time Step Truncation Error in Direct Simulation Monte Carlo", *Physics of Fluids*, Vol. 12, No. 10, 2000, pp. 2621–2633.

[13]Hadjiconstantinou, N. G., "Analysis of Discretization in the Direct Simulation Monte Carlo", *Physics of Fluids*, Vol. 12, No. 10, 2000, pp. 2634–2638

[14]Palharini, R. C., "Numerical Investigation of Aerothermodynamic in a Reentry Vehicle with Surface Discontinuity-Like Cavity", *MS Thesis*, National Institute for Space Research (INPE), Brazil, 2010.